AIAA Propulsion and Energy Forum
August 9-11, 2021, VIRTUAL EVENT
AIAA Propulsion and Energy 2021 Forum

10.2514/6.2021-3479

Design and Characterization of the Dual Independent Swirl Combustor Facility (DISCo)

Rahul Ramesh*, Sanjar Obidov†, Juan Paredes‡, Dennis S. Bernstein§, and Mirko Gamba¶
University of Michigan, Ann Arbor, MI 48109

The Dual Independent Swirl Combustor (DISCo) facility is a laboratory-scale gas turbine model combustor that is designed to exhibit thermoacoustic instabilities generated by the coupling of the unsteady combustion process with the acoustic properties of the combustion chamber and air/fuel plenums. The present work is aimed at discussing the design, hardware development, and characterization of the facility. Specifically, acoustic analysis performed to design the system and understand the dominant natural instability modes exhibited by it are presented. These are then validated through experiments. Additionally, a methane-air flame is studied through chemiluminescence measurements, and quantities such as time-averaged flame shape, intermittency, and Rayleigh Index are reported. This facility has been developed for combustion control studies. A demonstration of the interfacing of the facility with a secondary controller is also presented.

I. Introduction

Lean combustion has been the focus of most gas turbine combustion research over the last century. Its benefits with respect to reduced NOx content in the turbine's emissions has led to its widespread usage in both commercial power generation and the aviation sectors. However, these lean flames are susceptible to combustion instabilities such as flame extinction, re-ignition and thermoacoustic instabilities. In addition, introducing the air/fuel mixture into the combustion chamber with a swirl has been proven to stabilize the flames[1–4]. Although compact in nature, these swirling flames are characterized by complex interactions between flame dynamics, thermoacoustics, sheared swirling flows and high-intensity turbulence. Understanding the coupling between the thermoacoustic instabilities and its relation to hydrodynamic instabilities is imperative to designing highly efficient and stable combustors.

A number of swirl-stabilized combustor designs have been used to study premixed/partially premixed gas turbine combustors over the years. Stöhr et al. [5] gives a comprehensive literature survey of these swirlers. One of the most important parameters for a swirler is the swirl number (S) defined as the ratio of its axial flux of angular momentum to the axial flux of the axial momentum [3]. It is a measure of how fast a flow is spinning relative to how fast the bulk flow is moving. $S < 0.5$ is regarded as a weakly rotating flow while $S > 0.5$ is regarded as a strongly rotating flow. One of the widely studied swirl combustors includes the dual-swirl burner developed by Meier's group at DLR Stuttgart. This model combustor has been the target of extensive studies to investigate the flame dynamics and structure, thermoacoustic instabilities and more importantly, the coupling between the two phenomena. These studies were conducted primarily on methane-air flames. Additionally, Allison et al. [6] studied the combustor with a wider range of fuels such as syngas, propane, methane, and ethylene. Arndt et al. [7] studied a modified concentric dual-swirl burner where the air supplied to the inner and outer swirl nozzles are supplied from different plenums. Separation of the plenums supplying each swirl nozzles can be used to vary the mass-flow rates independently. This facilitates the definition of an air split ratio, $R = \dot{m}_{\mathrm{so}}/\dot{m}_{\mathrm{si}}$, where $\dot{m}_{\mathrm{so}}$ and $\dot{m}_{\mathrm{si}}$ are the mass-flow rates of air through the outer and inner swirler, respectively.

The current work describes a swirl combustor facility developed based on the design by Arndt et al. [7]. A limitation of their design is that the swirl number (S) is fixed by the design of the swirler and cannot be varied in real time. The combustor features a unique dual-swirl stabilized burner design that allows for the full control of the operation of the swirler, such as the air split ratio (R), and the strength of the swirling flow (S) in real time. For this reason, we refer to the system as the Dual Independent Swirl Combustor (DISCo). Figure 1 shows a three-dimensional rendering of the facility in the atmospheric and elevated pressure configurations.

*Graduate Research Assistant, rameshr@umich.edu Dept. of Aerospace Engineering.
†Research Engineer, Dept. of Aerospace Engineering.
‡PhD Candidate, Dept. of Aerospace Engineering.
§Professor, Dept. of Aerospace Engineering.
¶Associate Professor, Dept. of Aerospace Engineering, AIAA member.

The DISCo facility is developed to serve as a laboratory-scale gas turbine model combustor facility that replicates some of the characteristics of practical combustors. The aims of the study are to:

1) Experimentally investigate and quantify the effects of flow rate and swirl number on thermoacoustic instabilities in a concentric dual swirl burner configuration;
2) Develop a gas turbine model combustor to validate reduced-order CFD models; and
3) Study the effectiveness of external active control strategies to minimize the thermoacoustic instabilities that occur over the operating region of the combustor.

The external control strategy to be adapted in this study for minimizing combustion instabilities is based on the retrospective cost adaptive control (RCAC) algorithm. RCAC is a direct, discrete-time adaptive control technique for stabilization, command following, and disturbance rejection. RCAC was motivated by the concept of retrospectively optimized control, where past controller coefficients used to generate past control inputs are re-optimized in the sense that, if the re-optimized coefficients had been used over a previous window of operation, then the performance would have been better. However, unlike signal processing applications such as estimation and identification, it is impossible to change past control inputs, and thus the re-optimized controller coefficients are used only to generate the next control input. As a discrete-time approach, RCAC is motivated by the desire to implement control algorithms that operate at a fixed measurement sampling rate without the need for controller discretization. This discretization also means that the required modeling information can be estimated based on data sampled at the same rate as the control update.

For single-input, single-output linear systems, RCAC requires extremely limited modeling information, which consists of the sign of the leading coefficient and nonminimum-phase zeros. For multiple-input, multiple-output linear systems, RCAC uses impulse response matrices to capture nonminimum-phase transmission zeros. An overview of RCAC is given in [8], extension to include online system identification is developed in [9], and applications to systems with nonlinear dynamics are considered in [10–12]. The input signal to the controller is continuously acquired from the instrumentation and is used to establish the operating state of the device. The RCAC algorithm then determines how to properly adjust the output signals to maintain a desired state of operation of the device, which in this case, is to suppress thermoacoustic instabilities. The overarching goal of the study is to maintain a stable flame in a lean combustor while minimizing total emissions (NOx and CO_2) for a given thermal power output using parameters such as air split ratio (R) and inner and outer swirl numbers (S_i and S_o, respectively).

The focus of this study is to present an overview of the DISCo gas turbine model combustor facility and highlight the naturally occurring thermoacoustic modes exhibited by the system for a partially premixed methane-air flame. We first describe the design of the facility and the interfacing hardware developed to control the system. Next, acoustic analysis conducted in COMSOL to predict the system level response of the combustor is put forward and a comparison is drawn with experimental observations. Most importantly, the dominant modes exhibited by the facility are reported. Additionally, time-averaged flame shape, intermittency and Rayleigh index investigations carried out through OH^* and CH^* chemiluminescence studies are presented for a few cases.

With regard to the achieving the overarching aim of exercising secondary control strategies to reduce the instabilities in DISCo, initial efforts in developing the hardware and successful interfacing of DISCo with the RCAC controller demonstrated by manipulation of certain flow variables. The objective of the controller is to reduce pressure fluctuations in the combustion chamber. Further, to assess the performance of this controller in reducing the instabilities over the entire operational map of the combustor, a response map is being developed using the pressure fluctuations in the combustion chamber as a performance index.

II. Description of the DISCo Facility

A. Design Overview

The design of the Dual Independent Swirl Combustor facility is based on the following main goals: a) the ability to control the outer to inner swirler air split ratio (R) b) the ability to control the swirl number of the inner and outer swirler (S_i and S_o, respectively); and c) the ability to go to elevated pressure operation. To simulate realistic aircraft combustor and inflow environments, DISCo was designed to operate at pressures ranging from 1 to 15 atm with operating inlet temperatures ranging from 300 K to 600 K. For the work presented here, the facility is studied in its atmospheric pressure configuration, and thus details on the high-pressure configuration are not elaborated on here. The ranges of current operating conditions are presented in Table 1.

The combustor is developed with the ability to independently supply multiple air streams to independently change the swirl strength and air split ratio. Specifically, the mass-flow rate through the outer ($\dot{m}_\mathrm{so}$) and inner ($\dot{m}_\mathrm{si}$) swirlers are

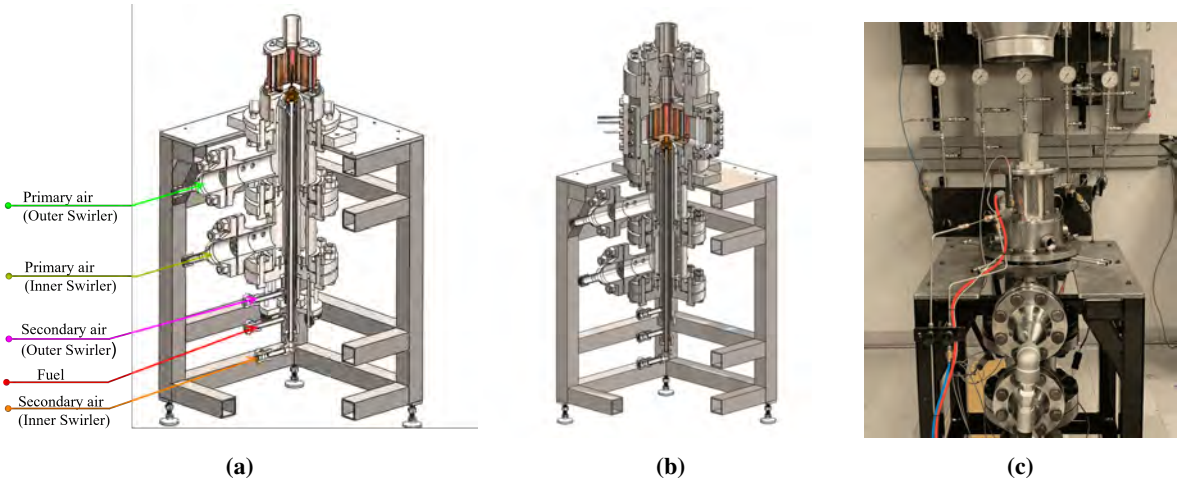

Fig. 1 Three-dimensional rendering of DISCo: (a) in the atmospheric pressure operation configuration; and (b) in elevated pressure operation configuration. (c) The commissioned DISCo facility in atmospheric condition.

Operating pressure, atm	Max. swirler air mass-flow rate, g/s	Equivalence ratio, ϕ
1	12	0.55-1.3

Table 1 Range of operating conditions of DISCo considered in this study.

manipulated independently, which result in the manipulation of the split ratio. Two secondary air supply lines to each of the swirlers then provide additional air flow to introduce axial flow to the inner ($\dot{m}_{\mathrm{ai}}$) and outer ($\dot{m}_{\mathrm{ao}}$) swirlers. These two additional supply lines allows us to manipulate the swirling ratio of the inner S_{i} and outer S_{o} swirlers independently. An additional supply line provides fuel to the burner and allows the manipulation of the equivalence ratio through changes in fuel mass-flow rate ($\dot{m}_{\mathrm{f}}$). This approach allows us to the independent control of all the quantities summarised in Table 2 using the novel dual swirler described next.

The novelty of the dual swirler used in DISCo lies in the addition of axial air injectors in each of inner and outer swirlers to alter the swirl number. Furthermore, the swirler was designed for 3-D printing. The most significant change is the use of square fuel injection holes instead of round holes. The swirler is fed by a total of five plenums corresponding to the five fluid paths described in the beginning of this section. These are letter labeled in Figure 2 as A: Outer Swirler, B: Inner Swirler, C: Secondary Air (Inner swirler), D: Secondary Air (Outer swirler) and E: Fuel.The swirler feeds the partially premixed fuel-air mixture into the combustion chamber.

The combustion chamber has a polygonal (octagonal) cross-section, is 126 mm tall and terminates into a constant area exit chimney 127 mm in length. A cross section of the combustion chamber and dual swirl nozzle is shown in Figure 2. The combustion chamber is composed of four water cooled posts made of copper that secure plates on all four sides. Solid metal plates or quartz windows can be used to provide optical access from all four sides. Solid metal plates can be used for providing wall surface instrumentation, such as for wall pressure measurements in different regions of the combustion chamber as required. In addition, the water cooled copper posts are instrumented with high-temperature microphones. Actively cooling of the combustion chamber is achieved through a closed water circuit.

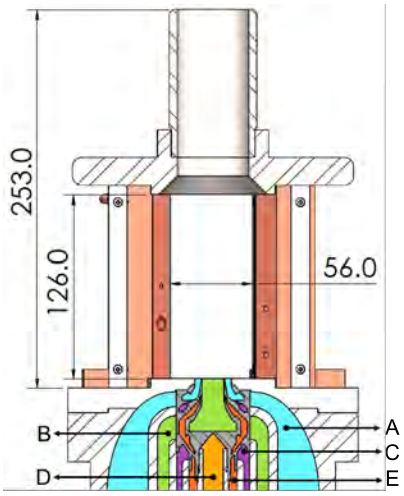

Fig. 2 A cut section view showing the different flowpaths through the novel swirler of DISCo.

Sl no	Quantity Varied	Variable
1	Total air mass-flow rate through combustor	$\dot{m}_a$
2	Equivalence ratio	ϕ
3	Outer-to-inner swirler air split ratio	R
4	Swirl number of the inner and outer swirler	S_i, S_o

Table 2 The offered control variables in DISCo.

B. Operation of DISCo and Hardware Infrastructure

DISCo is operated by a main control system (MCS) and data acquisition system (DAQ) developed using National Instruments (NI) hardware and a LABVIEW-based control program. A secondary adaptive control system (SACS) based on the RCAC algorithm (see Sec. I) is also present and it operates in tandem with the main controller. The secondary controller uses the same input/output interface. A set of custom-built electronic signal conditioners and switches have been developed to allow the interfacing and managing of the combustor, main and secondary controllers. The MCS is used for basic operation of the combustor, such as for ignition and steady state operation or otherwise basic open-loop controlled operation of the combustor. The SACS, instead, is used for closed-loop advanced control of the combustor, such for the suppression of undesired combustion instabilities. In essence, both the MCS and SACS possess similar control outputs to modify the state of operation of the device. When activated, the SACS continuously monitors the state of the combustor through feedback instrumentation (i.e., high-speed pressure sensors) and has the active ability to vary any of the controlling parameters as described previously to minimize the instabilities in the combustor. When SACS is active, the MCS simply serves as a supervisor controller to ensure safe operation. The mass-flow rates in each of the five fluid supply lines can be independently varied. This is accomplished by the use of independent air loaded pressure regulators coupled with electronic pressure controllers. The mass-flow rates are metered through the use of choked orifices immediately after the pressure regulators.

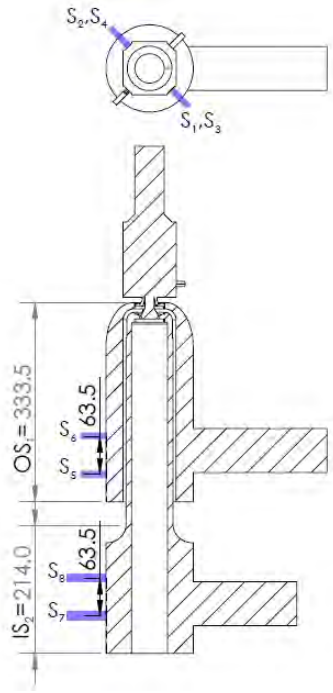

Fig. 3 Cut section view of the fluid volume showing the positioning of the different sensor ports.

The system has been adequately instrumented to measure the fluctuations in pressure in both the plenums and the combustion chamber as needed. Two sets of pressure transducers are used for these measurements: a) Two differential pressure transducers (Kulite type XCS-190L) with a sensitivity of 30 Pa/mV and maximum differential pressure of 1 atm; b) Two microphones (Kulite type MIC-190L) with a sensitivity of 9 Pa/mV. The sensitivities reported are calculated after the signal amplifier. These sensors are interchanged between measurement locations as required depending on the type of experiment being conducted. Figure 3 shows all the available sensor ports in the experiment. It should be noted that S_1 and S_2 are located at diagonally opposite posts of the combustion chamber at the same axial distance of 16 mm away from the base of the chamber. Sensors S_3 and S_4 are located 32 mm and 63.5 mm from sensors S_1 and S_2, respectively. The measurements from these sensors are acquired at a sampling rate of 15 kHz through a data acquisition system (NI PCIe-6343 multifunction I/O module).

To perform optical-based diagnostics of system, the solid metal plates in the combustion chamber are replaced by quartz windows. At the moment, we posses the ability to obatin the high-speed chemiluminescence measurements described in Section IV. The measurement of CH^* is performed using Phantom v711 high-speed camera using a band pass filter with wavelength 430 nm and FWHM of 10 nm. OH^* was measured with the Phantom TMX 5010 high-speed camera using a band pass filter of wavelength 310 nm with FWHM of 9 nm. The high-speed cameras and the pressure measurements are acquired at sample rates of 1.5 kHz and 15 kHz, respectively. Additionally, all the measurements are synchronized with each other and are triggered through a master trigger signal provided by the MCS of DISCo.

C. DISCo - RCAC Interface

A diagram of the DISCo - RCAC interface is shown in Figure 4, in which all signals represent electrical connections. A signal splitter is used to redirect the DISCo instrumentation measurements to both the MCS and SACS. The Control

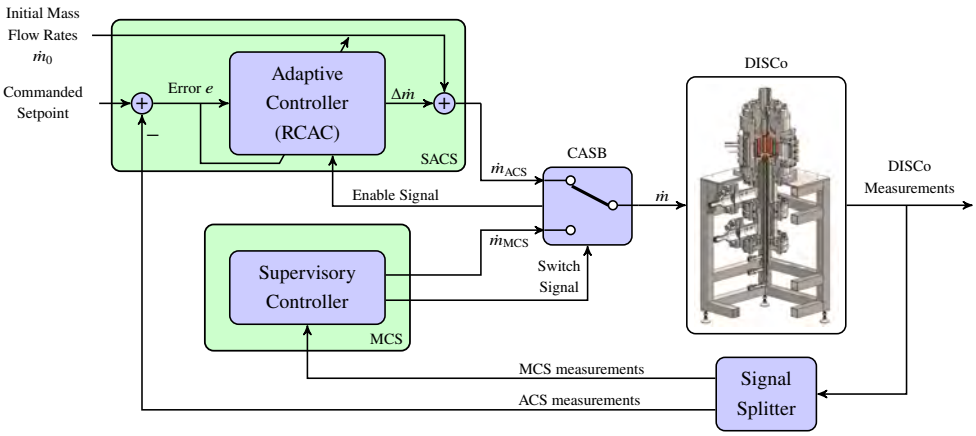

Fig. 4 DISCo - RCAC interface diagram. All signals represent electrical connections.

Algorithm Selection Box (CASB) acts as switch controlled by the MCS and determines which system has control over the combustor. The CASB also features low-pass filters that smooth any voltage mismatches that exist during transition between control systems. In all experiments, MCS controls the mass-flow rates in the beginning setting the initial operating point. A manual (human) input is then provided to the MCS when system is ready for transition. The CASB turns on the lowpass filter and switches the control from the MCS to the SACS. An enable signal from the CASB lets the SACS know that it now has control of DISCo. The lowpass filter is then turned off.

The input to the adaptive controller (RCAC) is given by the difference between a Commanded Setpoint and the measurements from the DISCo instrumentation. The output of RCAC is added to a set of initial mass-flow rates, which yields the commanded mass-flow rates. The purpose of this setup is to match the commanded mass-flow rates of the MCS and the SACS match when the MCS transfers control to the SACS. While the MCS has control over the DISCo facility, the output of RCAC is zero. The following sequence is followed in order to operate the SACS:

1) The MCS reaches a predetermined operating condition and a set of initial mass-flow rates are given to the SACS so that, when the MCS transfers control to the SACS, the mass-flow rates commanded by both systems match.
2) The MCS transfers control to the SACS, and RCAC determines the values of the commanded mass-flow rates.
3) Once the experiment is complete, control is transferred back to the MCS.

III. Acoustic Response of the System

Traditionally, combustion chambers are known to exhibit three modes of resonance. The most widely seen mode is the bulk Helmholtz mode with pressure being in phase across the volume of the resonator. A second plausible mode is a standing wave, which can be recognized by an amplitude variation through pressure nodes and anti-nodes. A third possibility exists through vortex shedding characterized by variations in the Strouhal number (St). These are summarized in detail in [13].

Schuller et al. [14] showed that the acoustic coupling between the plenums and the flame confinement tube is governed by a coupling index (Ξ) calculated based on the area ratio of the injector and the chamber and the temperature of the unburnt and burnt gases. This index can be used to establish the degree of coupling between the combustion chamber and the plenums in an existing system or serve as a basis to design new combustion systems that are fully decoupled. If $\Xi \leq 0.05$, it can be assumed that the plenum and combustion chamber are fully decoupled, whereas $0.05 < \Xi \leq 0.1$ implies they are weakly decoupled. They also note that the thermoacoustic coupling is controlled by elements that are upstream of the combustion chamber and preferentially to the plenum mode. In their case, the instability peak locked on to the plenumn Helmholtz resonance frequency at 140 Hz. Chen et al. [15] noted that the dominant instability mode of their system is a Helmholtz type at 310 Hz. Arndt et al. [7] noted multiple dominant thermoacoustic modes in their setup at 392 Hz and its second harmonic at 785 Hz. These were attributed to the longitudinal mode of the inner plenum through numerical studies and analytical calculations.

In this section, we apply the concepts used in the above studies to characterize the response of the swirl combustor. The value of Ξ for the system allows for the assumption that the thermoacoustic coupling will most likely be dominated by the elements that are upstream of the combustion chamber in the system, i.e., the inner and outer swirler plenums.

This is calculated using the combustion chamber cross sectional area, the inner and outer swirler cross sectional areas listed in Table **??**. The density and speed of sound of burnt gases used for the calculation are 0.18 kg/m^3 and 825 m/s, respectively. However, this index is not a sufficient parameter to infer which specific mode of the plenums the combustor will preferentially lock onto; and more specifically where the nodes/anti-nodes are located. An acoustic analysis was thus performed to predict these modes and their spatial locations.

A. Acoustic Analysis through COMSOL

The DISCo facility was designed to maximize the low-frequency acoustic response of the system from the design presented in [7] using COMSOL. Note that the geometry has two additional secondary air lines that allow for axial injection that are added to the respective plenums shown in Figure 1a. The acoustic analysis performed does not consider the fuel and secondary axial swirler lines because of their small cross sectional geometries at the swirler. The simulations were run to determine the lengths of the a) plenums; b) sidearms; and c) chimney shown in Fig. 1a to improve the low-frequency acoustics in the system. The variation of these parameters revealed the correspondence of the various modes observed in the system's frequency response to specific elements in the combustor. Analytical calculations are presented for these elements later for the final design for comparison. The frequency-domain studies were performed in the Acoustics module using the Pressure acoustics, Frequency Domain physics. A sound hard wall boundary was used on the internal fluid volume. The primary inner and outer swirler plenum sidearms were used as inlets. An unflanged circular pipe with waveguide end impedance was applied at the end face of the chimney to simulate a pressure outlet at STP conditions. The internal flow geometry of the combustor was split into two sections at the exit of the swirler: combustion chamber (CC) and the plenums in order to artificially introduce the combustion process by enforcing the speed of sound and density in the combustion chamber. Depending on the study performed, standard cold air or high-temperature air with a modified density was introduced into the combustion chamber. We refer to these cases as COLD and HOT runs, respectively.

The current studies were conducted assuming a stoichiometric mixture of methane and air. The higher temperature is implemented by raising the speed of sound (825 m/s) and lowering the density (0.18 kg/m^3) in the combustion chamber. For the rest of the fluid volume, an ambient temperature of 300 K is used.

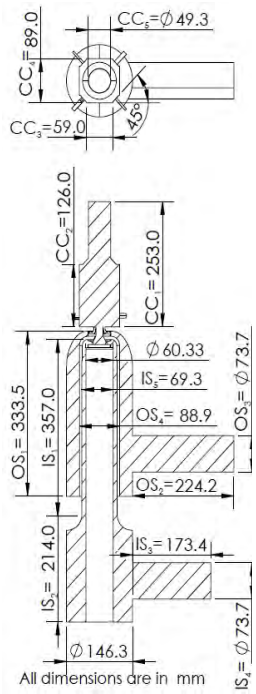

Fig. 5 Top view and cut section view of the fluid volume used in COMSOL.

Since the focus of this study was to study the eigenfrequencies, the mesh convergence studies involved identifying drastic changes in the frequency response of the domain in the interval [10, 1200] Hz. In this regard, physics-based meshes generated by COMSOL were used. For all the simulations presented, it was determined that having the software automatically generate an extra fine mesh was sufficient to capture the frequency response of the facility to the required accuracy. The generated mesh contained 228472 tetrahedra and 50280 triangular surface elements with a total volume of 9.574×10^{-3}m^3. The maximum element size was 0.0297 m and minimum size was 0.00127 m. The maximum allowed growth rate was 1.35, curvature factor was 0.3, and resolution of narrow regions was set to 0.85.

Modifications to the geometry were made such that the Helmholtz mode of the inner and outer swirl plenums matched more closely. Figure 6a shows the fluid volume meshed in COMSOL for the acoustic analysis. Figure 6d shows the frequency response of the volume presented in Figure 5 for both the HOT and COLD cases. Looking at the COLD case, we see a single peak response at around 130 Hz, which happens to be the bulk Helmholtz mode of the two plenums. A peak exists at around 256 Hz, which corresponds to a longitudinal quarter wave mode in the inner swirl plenum with a closed end indicated in the dimension IS$_1$ (see Figure 5). This longitudinal mode seems to be coupled with the Helmholtz frequency of the combustion chamber. A third low-amplitude peak is seen at around 315 Hz, which arises from the interaction of the inner swirl plenum and the swirler. The fourth peak at nearly 540 Hz corresponds to the longitudinal half-wave mode of the outer swirler. Although higher frequency peaks are observed near and above 700 Hz, which are usually harmonics of the lower frequency modes, we do not notice them in the swirl combustor facility experimentally. We support this statement with the findings in Section III.B.

Analytical calculations were also performed for the elements assuming planar waves and Helmholtz resonator behaviors, which served as a rough guide to understanding the physics of the combustor. These are compared to the

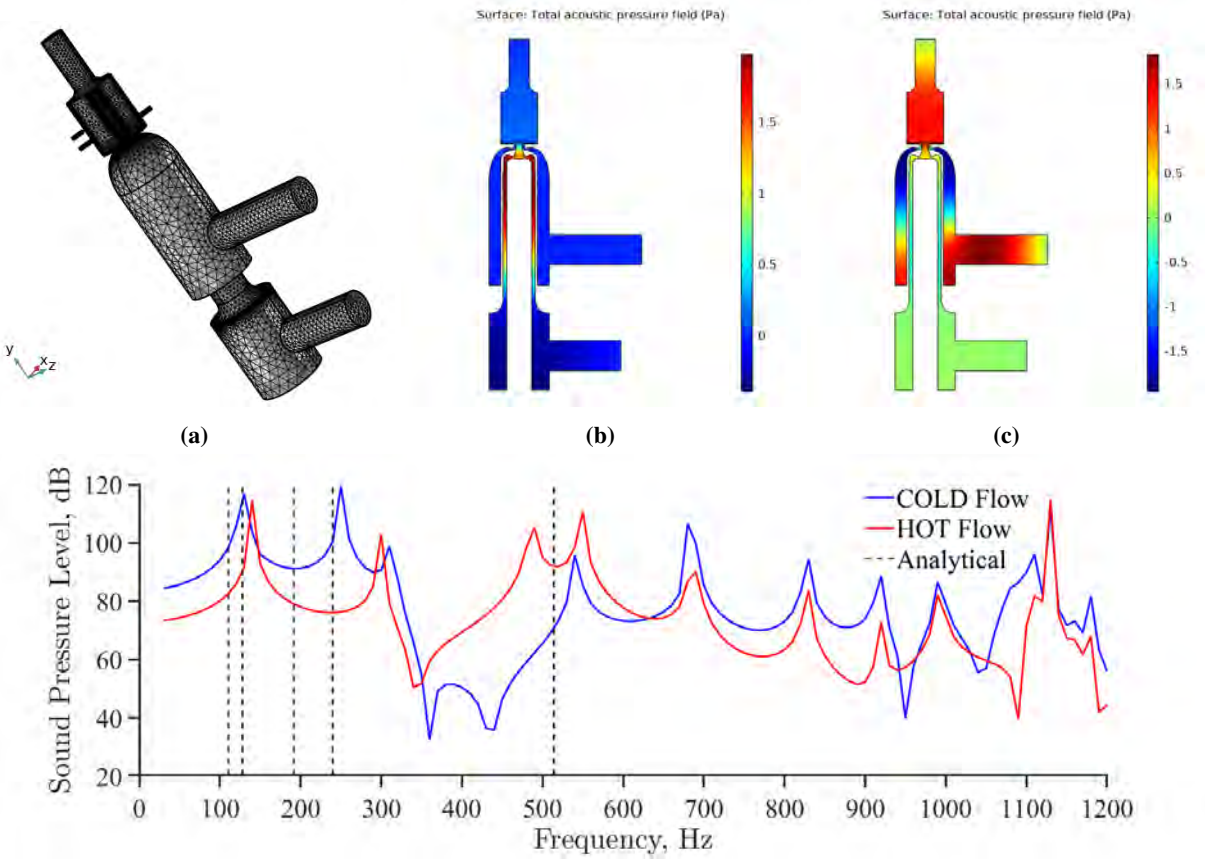

Fig. 6 Results of COMSOL studies showing a) mesh generated for the fluid volume; b) cross-sectional view showing the spatial distribution of the 300 Hz mode corresponding to the inner swirler (HOT Flow); c) cross-sectional view of the 550 Hz mode in the outer swirler (HOT Flow); and d) frequency response of the final geometry to COLD and HOT flow compared to analytical values (black vertical dash lines) presented in Table 3.

numerical simulations in Table 3 with the relevant dimensions used for each element. It should be noted that these values are calculated for the COLD case assuming the speed of sound as 343 m/s for all the elements. The inaccuracies to a few Hz can be attributed to variations in speed of sound properties and small geometries overlooked in the analytical calculations.

To understand the variation of acoustic eigenfrequencies with temperature, we refer to Figure 6d and turn our attention to the HOT case. We notice a negligible shift in the frequency spectrum for the Helmholtz resonance. However, the distributed peaks observed at around 250 and 310 Hz in the COLD case due to the inner swirl plenum form a distinct peak at 300 Hz. Note that the speed of sound is changed for combustion chamber in the HOT case and the Helmholtz frequency for this element is recalculated to be 460 Hz using a speed of sound of 825 m/s. Figure 6d shows that a new peak forms at around 507 Hz, which can be traced to be close to the Helmholtz resonance of the combustion chamber. A slight variation in the longitudinal half-wave mode of the outer swirler is observed at 540 Hz.

B. Experimental Validation of Acoustic Analysis

The various modes that could exist in the model combustor were summarized, and comparisons were drawn between numerical and analytical studies in Section III.A.

To complete the discussion, we now present experimental work that supports the studies mentioned above, and we analyze individual elements of the combustor. The initial tests on the facility were conducted in the atmospheric

Element	Relevant Dimensions	Mode	Frequency, Hz	
			Analytical Results	Numerical Results
Outer Swirler	OS_1	Longitudinal half wave	514	540
	OS_1,OS_2	Helmholtz	111	128
Inner swirler	IS_1	Longitudinal quarter wave	240	256, 315
	IS_1-IS_4	Helmholtz	128	143
Combustion Chamber	CC_1-CC_5	Helmholtz	192	256

Table 3 Summary of relevant acoustic modes obtained from analytical and numerical calculations of the fluid volumes for COLD flow.

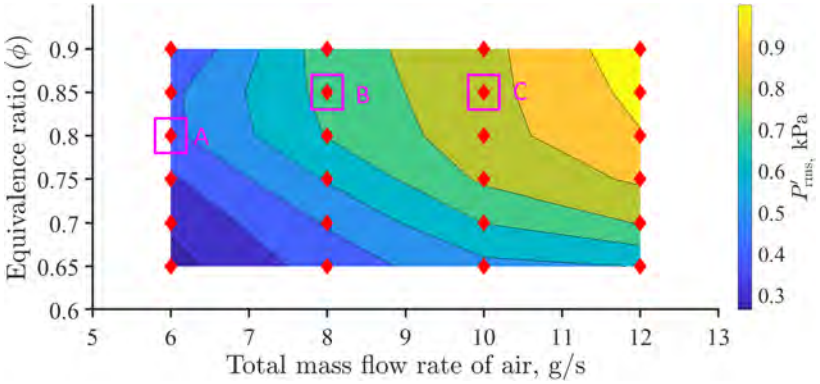

Fig. 7 Contour plot of P'_{rms} measured at location S_1 v/s $\dot{m}$ and ϕ for $R = 1.6$ in the current operating map of DISCo. Red diamonds indicate points of investigation in the test matrix. Pink squares represent cases considered for this study.

pressure condition over a range of mass-flow rates, equivalence ratios, and split ratio in order to understand the naturally exhibited instabilities of the device. The fuel used in these studies is methane. Initial measurements consisted of time-resolved dynamic pressure measurements acquired in the primary plenums and combustion chamber. The current test matrix involves the variation of equivalence ratio in increments of 0.05 from $\phi = 0.65$ to $\phi = 0.9$ for four different mass-flow rates from 6 g/s to 12 g/s in increments of 2 g/s. Figure 7 shows these points as a function of the pressure fluctuations measured in the combustion chamber in position S_1. From this test matrix, we present three cases of different mass-flow rates 6 g/s, 8 g/s, and 10 g/s (indicated as A, B, and C), which exhibit the typical behavior of the combustor for all studies presented in the current section and Section IV. These are cases are summarized in Table 4. The equivalence ratios for these cases are chosen according to the highest instability observed in the current test matrix for those mass-flow rates and $R = 1.6$ is maintained.

To identify any preferred instability mode, Fourier analysis, through the application of Fast Fourier Transform (FFT) of the time resolved pressure data was performed and the spectral content of the signal was analyzed. The power spectral density is calculated for using Welch's method using a hamming window with 50% overlap and sufficient resolution in frequency. These dominant modes are then compared to the COMSOL results.

In order to detect a longitudinal mode in the setup, we use the two sensor ports available in each element and examine any change in the root mean square of pressure fluctuation at the two locations. A Helmholtz mode is characterized by in phase pressure fluctuations measured between sensor ports that are separated by a distance in the system. To obtain this phase lag, the pressure fluctuations measured in different regions of the combustor were analyzed in the frequency domain using their cross power spectral density. For every experiment, the two signals are to be related and valid only if the value of their coherence was above 0.7 in the dominating frequency bins for the corresponding run (for example, compare the 293 and 585 Hz modes shown in Figure 8b). Unwrapping the cross power spectral density yielded information about the phase lag for the specific frequency bin (dominating bin was chosen) between the two signals. The same procedure is followed in order to analyze the phase lag between different elements of the combustor.

Case	$\dot{m}_a$ g/s	ϕ	Dominant Frequencies, Hz	Flame length, mm
A	6	0.8	266, 534	20
B	8	0.85	275, 550	30
C	10	0.85	277, 295, 556	42

Table 4 Chosen cases for the current study with their corresponding dominant frequencies and flame lengths. Note that $R = 1.6$ for all cases.

1. Identification of dominant instability modes

Figure 8 shows the time history and amplitude spectral density (ASD) of pressure fluctuations measured by one of the two MIC-190L sensors mounted in the combustion chamber (positions S_1 and S_2). The case presented also corresponds to the maximum instability case in the test matrix as shown by the contour plot in Figure 7. Two distinct peaks are observed in Figure 8b, the first with the highest amplitude at 293 Hz and a second dominant one at 585 Hz. These peaks seem to vary within 40 Hz across the range of conditions considered thus far. Both sensors at the two positions yielded similar results for each experiment and no frequency content was observed above 1 kHz and thus is not shown hereon for brevity.

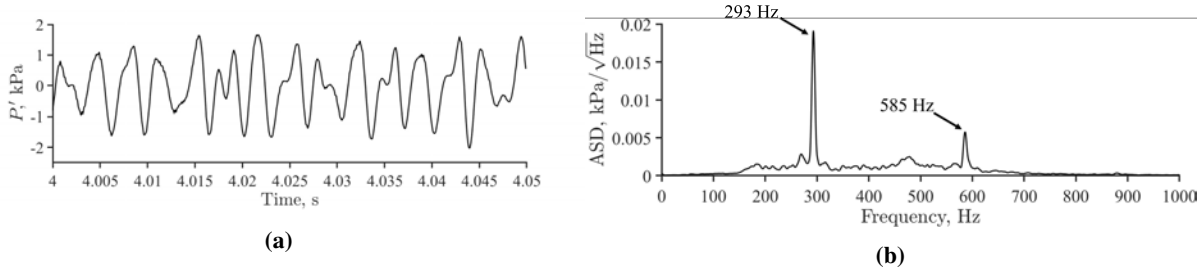

(a) **(b)**

Fig. 8 A typical experiment: (a) snippet of entire time trace of pressure fluctuation; and (b) an amplitude spectral density of the pressure signal obtained for total air mass-flow rate of 12 g/s, $\phi = 0.9$ and $R = 1.6$. The corresponding theoretical thermal power for this case is $P_{th} = 34.6$ kW.

Drawing comparisons with the HOT flow results presented in Figure 6d, we see that the dominant 293 Hz instability arises out of the quarter wave mode of the inner swirler. It should be noted that although the 585 Hz seems to be the second harmonic of the 293 Hz, it is mostly associated with the longitudinal mode of the outer swirler. The Helmholtz modes of the plenums do not appear in the power spectrum. This can be attributed to the resistance caused by the complicated internal flow path of the swirler. The combustion chamber's Helmholtz frequency was recalculated to be 460 Hz in Section III.A to account for HOT flow. Although, no distinct peak relating to this specific frequency in this specific experiment, we do notice that there are double peaks in the range of 500 Hz in other experiments that could be possibly related to this mode.

2. Element: Inner Swirler

In these experiments, MIC-190L sensors are mounted in position S_7 and S_8 as shown in Figure 3. We additionally instrument the combustion chamber with two XCS-190L differential pressure transducers in positions S_1 and S_2.

In Figure 9b, the sensor in the combustion chamber verifies the existence of two peaks in amplitude spectrum at 300 Hz and 550 Hz, respectively. The combustion chamber shows the highest peak in all cases. This is expected as the highest pressure fluctuations occur in this chamber. The inner swirler plenum is mildly responsive to the 275 Hz instability and remains indifferent to the 550 Hz mode as suggested by the numerical results presented in Figure 6c. The same characteristics were noticed for all the cases presented in Table 4. Additionally, Table 5 shows that the two sensors in S_7 and S_8 measure nearly the same P'_{rms} in the three cases. Such a behavior can be explained using Figure 6b and comparing the position of the sensor ports. The longitudinal mode of the inner swirler plenum is limited to the narrow cross section connected to the swirler as indicated by dimension IS_1 in Figure 3. Since the pressure measurements at these locations are consistent with the COMSOL simulations, we believe the quarter wave mode of the inner swirler is a driver for the lower frequency instability observed in the combustor.

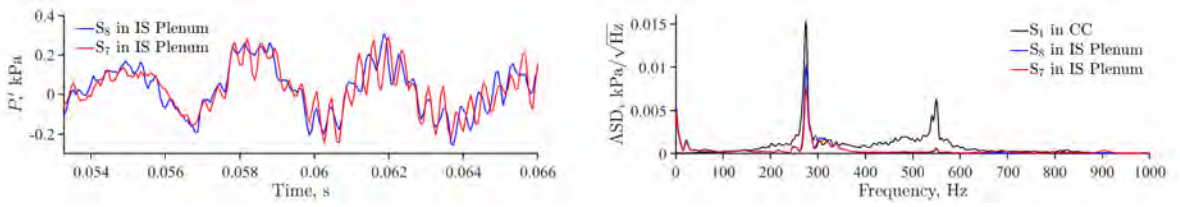

(a) (b)

Fig. 9 a) Time domain data from two sensor positions S_7 and S_8; and (b) Comparison of amplitude spectral density in the three sensor positions S_1, S_7 and S_8 for Case B presented in Table 4.

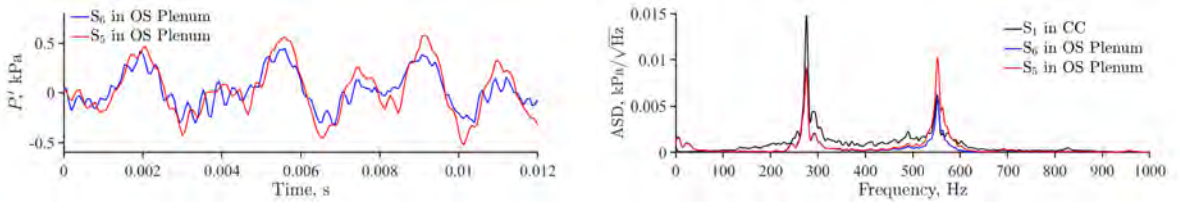

(a) (b)

Fig. 10 a) Time domain data of pressure fluctuations from two sensor positions S_5 and S_6; and (b) Comparison of amplitude spectral density in the three sensor positions S_1, S_5 and S_6 for Case B presented in Table 4.

3. Element: Outer Swirler

In these experiments, the two XCS-190L differential pressure transducers are mounted in positions S_5 and S_6 shown in Figure 3. The MIC-190L sensors are positioned in the combustion chamber at S_1 and S_2.

Figure 10b shows a sample amplitude spectrum of one of the three cases. It shows all sensors displaying the same peaks. Additionally, Table 5 compares the P'_{rms} in the two sensor locations. Here, Case A (6 g/s) shows a small variation in the P'_{rms} of the two sensors in the outer swirl plenum. This is expected as the 550 Hz mode is relatively weak in this case. As the mass-flow rate is increased through the outer swirler (Cases B and C), this mode increases in prominence and a larger variation in pressure amplitude is seen in these cases between the sensors. The variation in pressure amplitude is characteristic of a longitudinal mode and verifies its presence in the element.

4. Element: Combustion Chamber

In these experiments, we instrument the combustion chamber at different heights. Positions S_2 and S_4, which are 63.5 mm apart, house the MIC-190L sensors and positions S_1 and S_3, which are nearly 32 mm apart, house the XCS-190L transducers. With this positioning of the different sensors, we are able to correlate pressure measurements made along different positions along the axis of the combustion chamber prior to the chimney in diagonally opposite posts.

Cases	Inner Swirler		Outer Swirler	
	Sensor Position	P'_{rms}, kPa	Sensor Position	P'_{rms}, kPa
A	S_7	0.09	S_5	0.24
	S_8	0.07	S_6	0.25
B	S_7	0.15	S_5	0.24
	S_8	0.14	S_6	0.18
C	S_7	0.22	S_5	0.27
	S_8	0.21	S_6	0.20

Table 5 RMS fluctuation of pressure in the Inner and Outer Swirler plenum

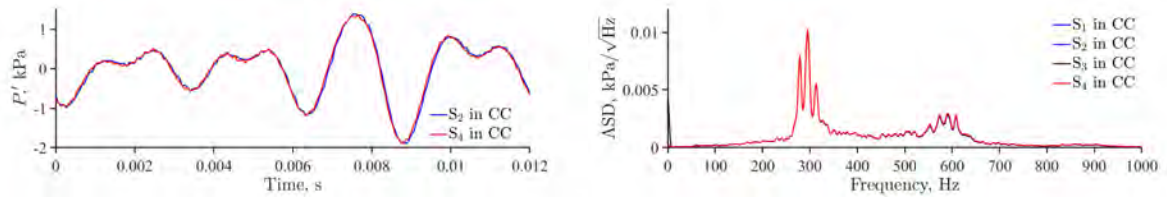

(a) **(b)**

Fig. 11 a) Time domain data of pressure fluctuations from two sensor positions S_2 and S_4 63.5 mm apart; and (b) Comparison of amplitude spectral density in the four sensor positions S_1, S_2, S_3 and S_4 for Case C presented in Table 4.

Table 6 shows the RMS fluctuation of pressure at different heights of the combustion chamber. It is seen that the pressure is nearly uniform throughout the combustion chamber when individual cases are considered which is characteristic of a bulk mode being present in this element. Additionally, phase delay measurements calculated through cross power spectral density of the two pairs of sensors revealed that there was negligible phase delay (within 10°) across all frequencies up to 1 kHz for the three cases. The time domain result presented in Figure 11a is reflective of this result. It should be noted that the Helmholtz mode of the combustion chamber occurs at 507 Hz for the HOT case according to the acoustic analysis. The resulting spectrum observed in the chamber could be a complex coupling of a bulk mode with the other longitudinal modes present in the system.

Cases	**Combustion Chamber**			
	Sensor Position	P'_{rms}**, kPa**	**Sensor Position**	P'_{rms}**, kPa**
A	S_2	0.44	S_1	0.45
	S_4	0.43	S_3	0.55
B	S_2	0.66	S_1	0.69
	S_4	0.65	S_3	0.68
C	S_2	0.84	S_1	0.88
	S_4	0.85	S_3	0.87

Table 6 RMS fluctuation of pressure in the Combustion Chamber.

5. Interaction Between Elements: Combustion Chamber, Outer and Inner Swirler

In the previous subsections, we have presented the element wise analysis of the combustor. We now present studies conducted to understand how the different elements in the system interact with each other. Specifically, we focus our attention to relating the combustion chamber to the outer swirler and the inner swirler, respectively. For this set of experiments, positions S_1 and S_2 were instrumented with MIC-190L sensors and S_5 and S_7 were instrumented with XCS-190L transducers, respectively.

Considering the combustion chamber and the outer swirler first, from the amplitude spectrum in Figure 12c, we can clearly see that the outer swirler's frequency response closely matches that of the combustion chamber. A comparison of the phase lag for the usual three cases is presented in Table 7. A positive phase lag implies that the combustion chamber pressure fluctuations leads the outer swirler. The time domain data from the two sensors presented in Figure 12a verifies this result. The dominant frequency component in case C yielded poor coherence and is not considered valid.

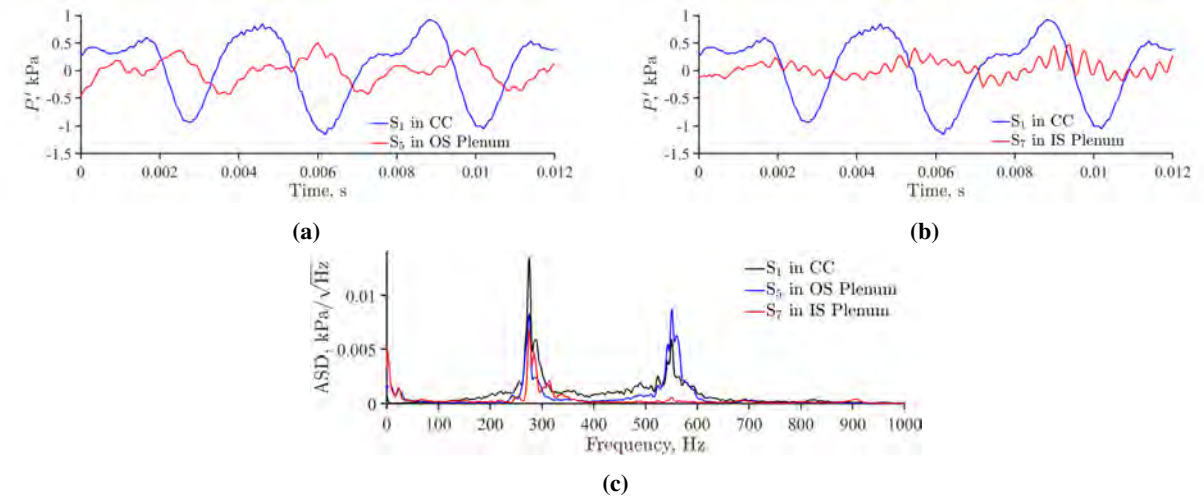

Fig. 12 a) Time domain data of pressure fluctuations from two sensor positions S_1 and S_5; (b) Time domain data of pressure fluctuations from two sensor positions S_1 and S_7; c) Comparison of amplitude spectral density in the three sensor positions S_1, S_5 and S_7 for Case B presented in Table 4.

Case	Dominant Frequencies, Hz	Phase Delay, degrees
A	266	112
	534	203
B	275	95
	550	165
C	275	169
	295	172

Table 7 Phase delay between S_1 and S_5 for cases presented in Table 4.

Finally, when evaluating the coupling between the combustion chamber and the inner swirler, a clear difference in the amplitude spectrum is seen in Figure 12c. The inner swirler is unresponsive to the 550 Hz component as before. Further, the time domain plot shown in Figure 12b also reveals that the IS is dominated by a significant amount of noise. This resulted in a poor coherence between sensors S_1 and S_7. With the current configuration of sensor positions, no conclusive remarks can be made relating to the phase difference between the combustion chamber and inner swirler. However, drawing from the conclusions obtained from the inner swirler elements analysis, we postulate that the quarter wave mode of the inner swirler influences the combustion chamber or vice versa. We plan to instrument the inner swirler at additional points close to the appearance of the longitudinal mode observed in the acoustic analysis in the future to understand this coupling.

IV. Flame Studies

In this section, quantities that are directly related to the flame dynamics, such as time-averaged flame position, intermittency, and Rayleigh index, are evaluated for the three cases presented in Table 4. As mentioned earlier, these three cases were chosen to study characteristics of the coupling between the reactive flow and the acoustic field. OH^* chemiluminescence can be correlated to heat release fluctuations [16] in the combustor which can dampen or strengthen the thermoacoustic instabilities. Since the fuel used for the current experiments is CH_4, CH^* chemiluminescence can also be used as an additional flame marker for these studies. Hence, OH^* and CH^* chemiluminescence measurements are used in this study to understand the dynamics of the combustion process. The experimental setup used for these studies is described in Section II.B.

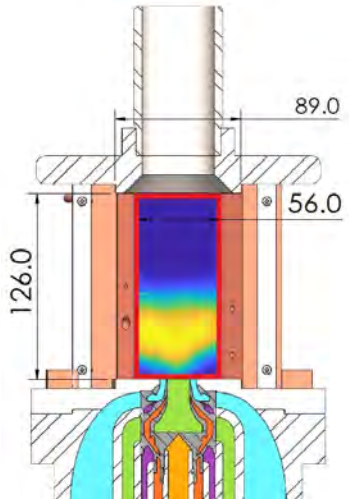

Fig. 13 Chemiluminescence field of view representation in the combustion chamber denoted by the red rectangle.

First, the flame distribution, shape and its fluctuation are analyzed. CH^* chemiluminescence emission is used to identify the distribution of the flame and to construct measures of the probability of finding the flame at a given point within the field of view. Using each frame from the high-speed movies, flame position is found by binarizing each frame using a threshold value determined using Otsu's method [17], which is a histogram-based technique, applied to the full set of data. Otsu's method [17] segments an image into two components, object and background, by bisecting the histogram into two classes and calculating the statistical variance between them. All pixels above the threshold are assigned 1, while those below the threshold are assigned 0. Once the set of images is binarized, a time average of the binarized images is computed. We refer to this time-averaged image as π. Essentially, this approach yield a measure of the probability of locally finding the flame. Figure 14 shows the resulting time-averaged flame position for the three cases studied. The axis of the images are normalized by width (W = 89 mm) and height (H = 126 mm) of the combustion chamber.

From Figure 14 we gather a general shape and spatial distribution of the flame. The effective length of the flame increases with mass-flow rate and the upper surface becomes flatter. The cumulative distribution function (CDF) is used to evaluate the effective lengths of the flame. The upper and lower boundaries used for the calculation of flame length from the CDF are set as 90% and 10%, respectively. The results of this study are presented in Table 4.

In addition, a measure of flame intermittency is used to provide a representation of regions where flame front moves. Flame intermittency is defined by

$$\epsilon = \frac{1}{T}\sum_{t}\left(B[t]-\pi\right)^2, \tag{1}$$

where $B[t]$ is the binarized image and π is time average of all binarized frames. As shown in Figure 15, $\epsilon = 0$ indicates no variability in the position of the flame, while an increasing value of ϵ indicates a highly fluctuating flame front.

The Rayleigh index (Ra) can provide considerable insights into combustion dynamics and the mechanism leading to thermoacoustic instabilities. These instabilities can grow in amplitude as long as the energy transfer into the coupling mechanism is greater than the energy lost due to damping. The Rayleigh index is defined as

$$\mathrm{Ra}(x,y) = \frac{1}{T}\int_0^T \frac{P'(x,y,t)q\prime(x,y,t)}{P'_{\mathrm{rms}}q'_{\mathrm{rms}}}\mathrm{d}t, \tag{2}$$

where $P'(x,y,t)$ and $q'(x,y,t)$ are the fluctuating components of the pressure and heat release rate within the combustion chamber, respectively. The corresponding root mean square values are defined by P'_{rms} and q'_{rms}. A positive Ra indicates that the heat release rate and pressure oscillations are coupled in phase. A negative Ra indicate that the heat release rate and pressure oscillations are out of phase and thus the instabilities are generally damped. As discussed in Section III.B.4 pressure measurements at different points within the combustion chamber showed acoustic oscillations are spatially invariant, thus a single pressure measurement is sufficient to characterize the pressure oscillation of the entire combustion chamber. A microphone (Kulite MIC 190L) located at position S_1 in Figure 3 is used in this regard.

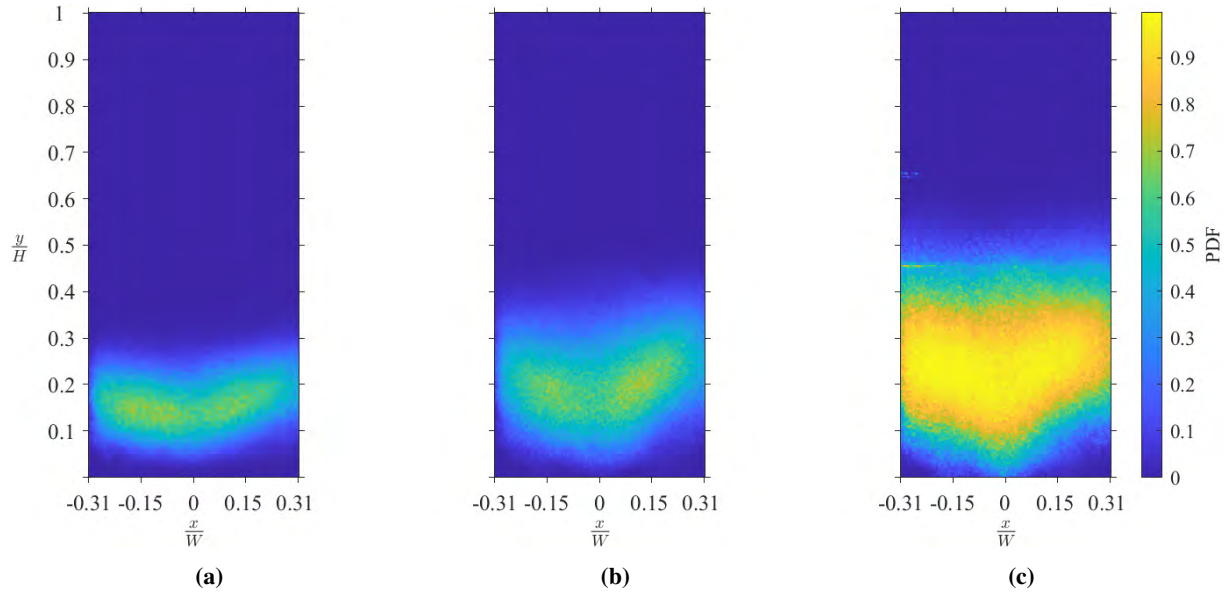

Fig. 14 Probability density function of the flame calculated from CH* chemiluminescence: (a) Case A; (b) Case B; (c) Case C.

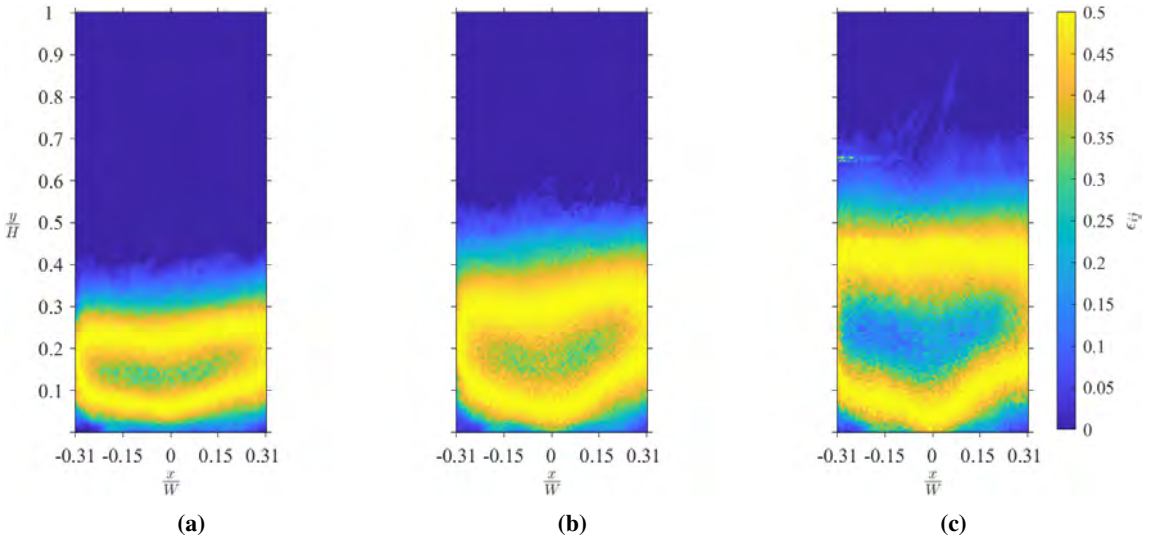

Fig. 15 Intermittency of the flames calculated from CH* chemiluminescence: (a) Case A; (b) Case B; (c) Case C.

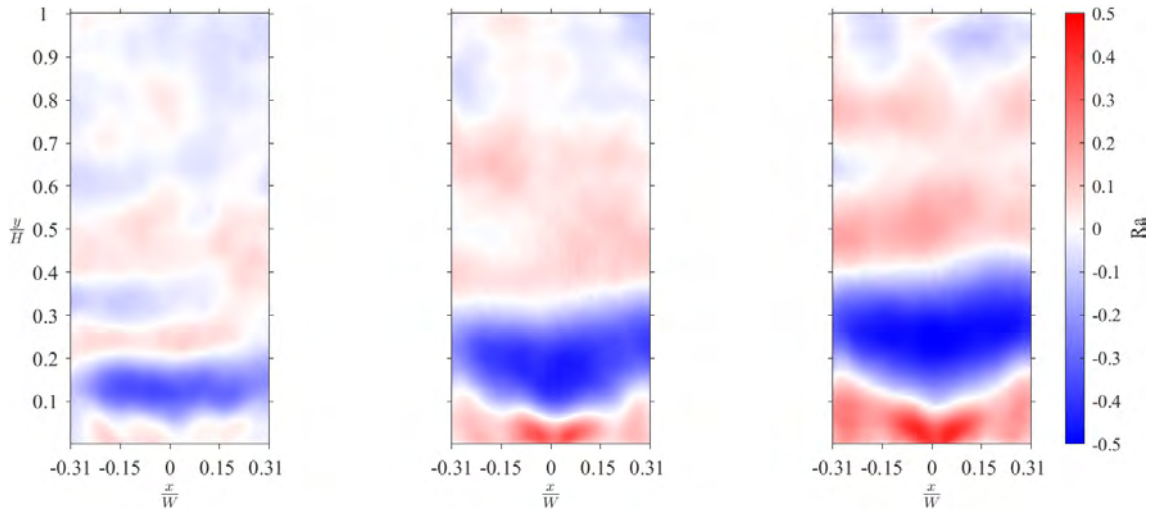

Fig. 16 Ra calculated from pressure at position S_1 and OH^* chemiluminescence for: (a) Case A; (b) Case B; (c) Case C.

Figure 16 shows that the highest positive Rayleigh index is observed close to the swirler, near the floor of the combustor, whereas the most negative region is located within the flame itself. However, additional work needs to be carried out to fully characterize the coupling between the heat release and pressure fluctuations.

The results shown previously contained time domain information of the flame. We now present a comparison of the high-speed imaging data to the pressure sensor data in the frequency domain. In order to do this, an average pixel intensity defined over a small region of interest (RoI) of the CH* emission image (15x15 pixels) is used. The region of interest is defined and shown in Figure 17b. This specific point is chosen because this region has the highest value of intermittency. From the time trace of the CH* emission intensity a corresponding ASD is computed. Referring back to Table 4 where the dominant frequencies from the pressure measurement were summarized, we found dominant frequencies at 266 and 534 Hz for Case A. The frequency peaks observed in the CH* chemiluminescence emissions as shown in Figure 17a compare well with their corresponding pressure counterparts confirming that the flame responds to both the 266 and 534 Hz modes.

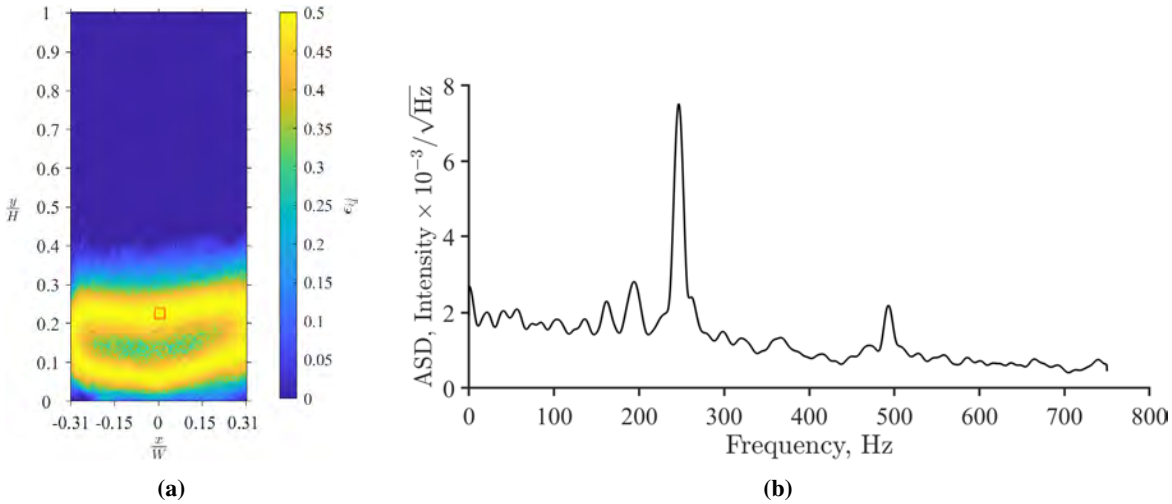

Fig. 17 (a) RoI for ASD computation. (b) Spectral Density from CH* chemiluminescence for case A.

V. Demonstration of the Use of Secondary Controller to Manipulate DISCo

As mentioned at the end of Sec. I, the end goal of the experiment is to develop a model combustor system that can interface with secondary controllers to achieve an objective such as a stable flame in a lean combustor while minimizing emissions. Note that the four available control variables of DISCo are listed in Table 2. As a first step in achieving this goal, this section demonstrates the manipulation of DISCo through the RCAC control algorithm. The objective of the controller for the tests presented here is to reduce the pressure fluctuations (P') measured with MIC-190L microphone in the combustion chamber at position S_1. A reduction of the pressure oscillations corresponds to a more stable flame leading to the choice of this variable. The initial tests focus on reaching steady state solutions of the controller algorithm while manipulating a single variable in order to simplify the control task. The first set involves the manipulation of ϕ by controlling the mass-flow rate of fuel ($\dot{m}_f$) while R and thus $\dot{m}_a$ is kept constant. The limits on ϕ were specified as $0.65 \leq \phi \leq 0.9$ so as to prevent blowoff/rich mixtures. Conversely, in the second set, R and thus $\dot{m}_{si}$ and $\dot{m}_{so}$ are manipulated while $\dot{m}_f$ and $\dot{m}_a$ are kept constant.

The results of a single test from each set are displayed in Figures 18 and and 19. In both cases, $\dot{m}_a = 6$ g/s. In the case where R is kept constant, $R = 1.32$. In the case where ϕ is kept constant, $\phi = 0.8$. The initial point presented is the point of maximum instability for a total air mass-flow rate of 6 g/s. As shown in Figures 18a and 19a, in both instances, RCAC manages to reduce the value of P'_{rms}, and thus RCAC reaches a steady state solution where the combustor instabilities are reduced. The adaptation coefficients of RCAC are denoted as θ. Initially, θ is a 0 vector. The values of θ change as RCAC receives more data and determine the output of the adaptive controller. Figures 18d and 19d show the values of θ over time for both tests, which show how RCAC settles down after reaching a steady state solution.

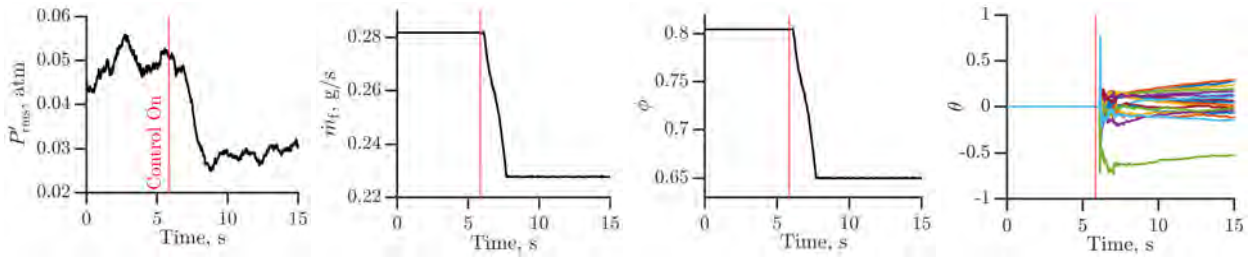

(a) **(b)** **(c)** **(d)**

Fig. 18 RCAC test results in the case where ϕ is manipulated and $\dot{m}_a$ and R are kept constant, where $\dot{m}_a = 6$ g/s and $R = 1.32$. Time domain data is shown for (a) P'_{rms}, (b) $\dot{m}_f$, (c) ϕ, and (d) θ, the adaptation coefficients of RCAC. The vertical red line denotes the enabling of the RCAC algorithm.

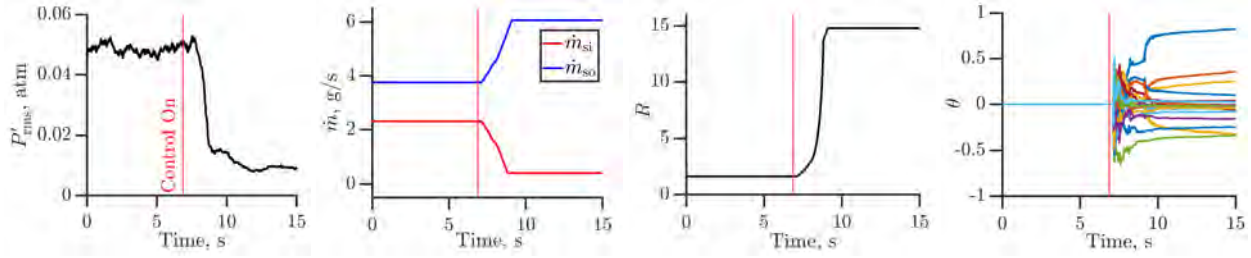

(a) **(b)** **(c)** **(d)**

Fig. 19 RCAC test results in the case where R is manipulated and ϕ and $\dot{m}_a$ are kept constant, where $\dot{m}_a = 6$ g/s and $\phi = 0.8$. (a) P'_{rms}, (b) $\dot{m}_{si}$ and $\dot{m}_{so}$, (c) R, and (d) θ, the adaptation coefficients of RCAC. The vertical red line denotes the enabling of the RCAC algorithm.

Figure 20 shows a different, more intuitive representation of results obtained from the test shown in Figure 18. It shows the path followed by the RCAC alogirthm during the experiment in the control variables and objective space(ϕ and P'_{rms}, respectively). The final state reached by the controller is a reduction in equivalence ratio to $\phi = 0.65$ which is the manually specified lean blowout limit. A reduction in P'_{rms} is seen through this path. These results demonstrate the capability of the RCAC algorithm to manipulate the flow variables of DISCo.

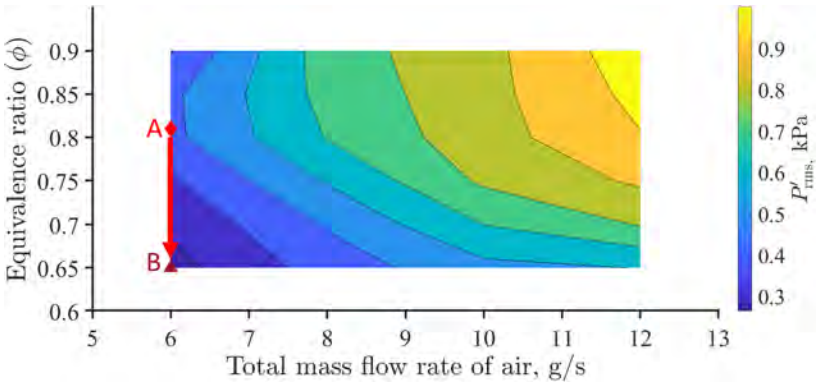

Fig. 20 Path followed by the RCAC controller to reduce P'_{rms}. Note: Red diamond (A) represents the initial point, red arrow head denotes the path and the brown triangle (B) shows the final point.

VI. Conclusions and Future Work

We have presented here a detailed description and characterization of the DISCo facility. Details relating to the design of the facility, specifically the swirler and the hardware infrastructure developed to interface with a secondary controller is presented. A detailed analysis relating to the acoustic response of the system is presented and comparison are drawn between analytical calculations, COMSOL simulations and experiments. It was seen that the COMSOL simulations are able to predict the different modes appearing in the system with accuracy. The dominant modes of the system are characterized to be the quarter wave mode of the inner swirler at nearly 300 Hz and the longitudinal mode of the outer swirler at 585 Hz for the maximum instability case in the test matrix. Further, for three specific cases which reflect the typical behaviour of the combustor, element wise studies were conducted to verify the existence of these modes. Phase difference studies between different elements led to the conclusion that the pressure dynamics of the combustion chamber leads that of the outer swirler plenum and influences its longitudinal mode. This phase delay is seen to vary with different mass-flow rates and equivalence ratios. Conclusive remarks regarding the interaction between the inner swirler and the combustion chamber could not be drawn due to the location of measurement points. Additionally, OH^* and CH^* chemiluminescence studies revealed the flame location and shape. Important parameters, such as the flame intermittency and the Rayleigh index, are presented for three cases. Finally, the ability of the DISCo facility to interface with a secondary controller is demonstrated.

We plan on adding additional measurement points in the combustor with the objective of understanding the interaction between the inner swirler and the combustion chamber. With regard to the RCAC secondary controller, we plan to breakdown the control problem of maintain a stable flame in DISCo while minimizing thermoacoustic instabilities and reducing emissions into phases of increasing complexity. Additionally, an assessment tool will be developed using Design of Experiments methods to evaluate the performance of the control algorithm.

Acknowledgments

This research was supported by NSF grant CMMI 1634709.

References

[1] Syred, N., Chigier, N., and Beér, J., "Flame stabilization in recirculation zones of jets with swirl," *Symposium (International) on Combustion*, Vol. 13, No. 1, 1971, pp. 617–624. https://doi.org/10.1016/s0082-0784(71)80063-2, URL https://doi.org/10.1016/s0082-0784(71)80063-2.

[2] Syred, N., and Beér, J., "Combustion in swirling flows: A review," *Combustion and Flame*, Vol. 23, No. 2, 1974, pp. 143–201. https://doi.org/10.1016/0010-2180(74)90057-1, URL https://doi.org/10.1016/0010-2180(74)90057-1.

[3] Gupta, A. K., Lilley, D. G., and Syred, N., *Swirl flows*, Abacus Press, 1984.

[4] Weigand, P., Meier, W., Duan, X., Stricker, W., and Aigner, M., "Investigations of swirl flames in a gas turbine model combustor," *Combustion and Flame*, Vol. 144, No. 1-2, 2006, pp. 205–224. https://doi.org/10.1016/j.combustflame.2005.07.010, URL https://doi.org/10.1016/j.combustflame.2005.07.010.

[5] Stöhr, M., Boxx, I., Carter, C. D., and Meier, W., "Experimental study of vortex-flame interaction in a gas turbine model combustor," *Combustion and Flame*, Vol. 159, No. 8, 2012, pp. 2636–2649. https://doi.org/10.1016/j.combustflame.2012.03.020, URL https://doi.org/10.1016/j.combustflame.2012.03.020.

[6] Allison, P. M., Driscoll, J. F., and Ihme, M., "Acoustic characterization of a partially-premixed gas turbine model combustor: Syngas and hydrocarbon fuel comparisons," *Proceedings of the Combustion Institute*, Vol. 34, No. 2, 2013, pp. 3145–3153. https://doi.org/10.1016/j.proci.2012.06.157, URL https://doi.org/10.1016/j.proci.2012.06.157.

[7] Arndt, C. M., Severin, M., Dem, C., Stöhr, M., Steinberg, A. M., and Meier, W., "Experimental analysis of thermo-acoustic instabilities in a generic gas turbine combustor by phase-correlated PIV, chemiluminescence, and laser Raman scattering measurements," *Experiments in Fluids*, Vol. 56, No. 4, 2015. https://doi.org/10.1007/s00348-015-1929-3, URL https://doi.org/10.1007/s00348-015-1929-3.

[8] Rahman, Y., Xie, A., and Bernstein, D. S., "Retrospective Cost Adaptive Control: Pole Placement, Frequency Response, and Connections with LQG Control," *IEEE Contr. Sys. Mag.*, Vol. 37, No. 5, 2017, pp. 28–69.

[9] Islam, S. A. U., Nguyen, T. W., Kolmanovsky, I. V., and Bernstein, D. S., "Data-Driven Retrospective Cost Adaptive Control for Flight Control Application," *Journal of Guidance, Control, and Dynamics*, 2021. To appear; also arXiv 2102.07191.

[10] Islam, S. A. U., and Bernstein, D. S., "Output-Feedback Adaptive Control of Discrete-Time Systems with Unknown, Unmatched, Inaccessible Nonlinearities," *Proc. Amer. Contr. Conf.*, Milwaukee, WI, 2018, pp. 1695–1700.

[11] Kamaldar, M., Islam, S. A. U., Sanjeevini, S., Goel, A., Hoagg, J. B., and Bernstein, D. S., "Adaptive Digital PID Control of Sampled-Data Systems with First-Order-Lag-Plus-Dead-Time Dynamics and Sensor, Actuator, and Feedback Nonlinearities," *Adv. Control Appl.*, Vol. 1, 2019, pp. 1–46.

[12] Goel, A., Duraisamy, K., and Bernstein, D. S., "Retrospective Cost Adaptive Control of Unstart in a Model Scramjet Combustor," *AIAA J.*, Vol. 56, No. 3, 2018, pp. 1085–1096.

[13] Lieuwen, T. C., *Unsteady Combustor Physics*, Cambridge University Press, 2012. https://doi.org/10.1017/cbo9781139059961, URL https://doi.org/10.1017/cbo9781139059961.

[14] Schuller, T., Durox, D., Palies, P., and Candel, S., "Acoustic decoupling of longitudinal modes in generic combustion systems," *Combustion and Flame*, Vol. 159, No. 5, 2012, pp. 1921–1931. https://doi.org/https://doi.org/10.1016/j.combustflame.2012.01.010.

[15] Chen, Y., and Driscoll, J. F., "Experimental Studies and Modeling of Acoustic Instabilities in a Gas Turbine Model Combustor," *53rd AIAA Aerospace Sciences Meeting*, American Institute of Aeronautics and Astronautics, 2015. https://doi.org/10.2514/6.2015-1566, URL https://doi.org/10.2514/6.2015-1566.

[16] Lauer, M., and Sattelmayer, T., "On the Adequacy of Chemiluminescence as a Measure for Heat Release in Turbulent Flames With Mixture Gradients," *Journal of Engineering for Gas Turbines and Power*, Vol. 132, No. 6, 2010. https://doi.org/10.1115/1.4000126, URL https://doi.org/10.1115/1.4000126.

[17] Otsu, N., "A Threshold Selection Method from Gray-Level Histograms," *IEEE Transactions on Systems, Man, and Cybernetics*, Vol. 9, No. 1, 1979, pp. 62–66. https://doi.org/10.1109/TSMC.1979.4310076.